Ultrafast Science
A SCIENCE PARTNER JOURNAL

RESEARCH ARTICLE

Two-Photon Pumped Phase Locking of Random Lasers in Hybrid Perovskite Multi-Crystalline Microdisks

Qin Zhang, Yue Liu, Yi Zhang, Yuxin Zhang, Jinxin Guo, Yiwei Zhang, Yulan Fu*, and Xinping Zhang*

School of Physics and Optoelectronic Engineering, Institute of Information Photonics Technology, Beijing University of Technology, Beijing 100124, P. R. China.

*Address correspondence to: fuyl@bjut.edu.cn (Y.F.); zhangxinping@bjut.edu.cn (X.Z.)

Citation: Zhang Q, Liu Y, Zhang Y, Zhang Y, Guo J, Zhang Y, Fu Y, Zhang X. Two-Photon Pumped Phase Locking of Random Lasers in Hybrid Perovskite Multi-Crystalline Microdisks. *Ultrafast Sci.* 2024;4:Article 0068. https://doi.org/10.34133/ultrafastscience.0068

Submitted 1 February 2024
Accepted 14 June 2024
Published 29 July 2024

Phase control of random lasing processes has been a challenge both in physics and in the device/materials design. Although conventional saturable absorbers can be integrated with random lasers to conceive mode-locking scheme, low intensity and random directions of the lasing radiation reduce largely the possibility. In such considerations, we put forth a new mode-locking mechanism, which is defined as cascaded absorption and stimulated emission (CASE), and have it achieved in multicrystalline microdisk structures of a hybrid perovskite. This scheme applies only to lasing materials with strong overlap between the absorption and emission spectra. In this work, we employed 2-photon pumping at 800 nm with a pulse duration of about 150 fs to realize phase-locked random lasing in $MAPbBr_3$ microdisks in donut shapes, which are produced by micro-imprinting using a flexibly transferred template of tricyclo[5.2.1.$0^{2,6}$] decanedimethanol diacrylate. The phase-locking performance is identified by the narrow-band lasing lines with equal separations. The constant phase shift for initializing phase locking is determined by the internal conversion lifetime in the $MAPbBr_3$ molecules. Two-photon pumping enables large penetration depth into the microdisks and consequently large numbers of phase-locked lasing modes, producing much narrowed and high-contrasted spectral lines. Lasing lines with a bandwidth as narrow as 0.26 to 0.3 nm and an equal separation ranging from 1.7 to 4.8 nm have been achieved for different microdisk schemes. These results imply marked progress in new random lasing physics and potential applications in ultrafast laser technology.

Introduction

Random lasers have been achieved in various materials with differently designed random scattering structures [1–8], which have potential applications in incoherent imaging [9,10], laser illumination [11,12], display [13–15], and sensing [16,17]. Broad-band [1,2] or multipeak [18–20] output spectrum is the most typical characteristics. The randomness in this type of lasers lies not only in the random distributions of the scattering structures and the random directions of light propagation that determine the optical gain channels but also in the random phase relationship between the lasing modes. Phase locking of the random lasers has been a challenge for both material science and laser physics so that direct experimental observation of the phase-locking performance of random lasers has rarely been reported.

Saturable absorbers (SAs) are the most extensively employed approach for realizing mode locking of various conventional lasers. Semiconductors [21–24] and 2-dimensional (2D) materials [25–27], including topological insulators [28–31], are typical SA candidates. Integration of SA with the random laser scheme is the most convenient and can be considered as the most feasible strategy for achieving phase locking of random lasers. However, the required light intensity for saturated absorption is difficult to reach in random lasers, which restricts largely the application of conventional mode-locking techniques based on SA in random lasing devices.

Multiple research attempts have been demonstrated both theoretically [32,33] and experimentally [34,35] in different materials with different structural designs to investigate phase locking of random lasers. However, there have been no direct observations of experimental features of phase-locked random lasers. Using a sophistically designed pumping scheme, the number of activated modes can be selectively controlled in a random laser, which has been taken as a phase-locking transition [33,34]. In combination with SA materials, mode-locking mechanism has been proposed in electrically pumped random lasers in the far infrared [35].

In our recent publication, we put forth a new phase-locking mechanism based on the strongly overlapped absorption and emission spectra in the laser gain medium [36], which is defined as cascaded absorption and stimulated emission (CASE). This is a first direct observation of phase-locked random lasers. In this work, we employed a 2-photon pumping scheme, which leads to a large penetration depth of the pump pulses into the

gain medium so that an increased number of laser channels and much enhanced phase-locking mechanisms have been achieved, as compared with the single-photon pumping scheme. As a result, much narrowed linewidth and much enhanced contrast are produced in the output lasing lines, evidencing further the CASE mechanisms. This is a significant contribution to both the laser physics and the advancement of random lasers.

Square Lattices of Multicrystalline $MAPbBr_3$ Microdisks as Random Lasers

Fabrication procedures for producing 2D $MAPbBr_3$ square lattices are shown in Fig. 1A. An indium tin oxide (ITO) glass plate with a dimension of 20×20 mm^2 is ultrasonically cleaned sequentially by deionized water, acetone, and anhydrous ethanol for 30 min. The S1805 photoresist (PR; from Rohm & Haas Electronic Materials Ltd.) was spin-coated onto the cleaned ITO glass at a speed of 1,500 rpm for 30 s, as shown in Fig. 1A①. The PR/ITO glass sample was heated on a hotplate at 115 °C for 60 s before a 2-step photolithography process, where the sample was exposed to an ultraviolet (UV) light beam for 15 s and the mask was rotated by 90° in the second exposure, as shown in Fig. 1A②. After the development and rinsing processes, a 2D PR grating consisting of square columns was produced, as shown in Fig. 1A③.

To avoid the dissolution of S1805 PR in the solvent of *N*,*N*-dimethylformamide (DMF), we need to transfer the 2D lattices into tricyclo[5.2.1.$0^{2,6}$] decanedimethanol diacrylate (ADCP) by a micro-imprinting approach, as shown in Fig. 1A④, where 0.7 g of ADCP, 0.3 g of dipentaerythritol penta-/hexa-acrylate, and 5 mg of 2,2-dimethoxy-2-phenylacetophenone (DMPA) were mixed and stirred under red light for 2 h to produce a transparent precursor solution. The 2D PR grating was used as the stamp and was pressed tightly onto a droplet of ADCP solution on a piece of cleaned ITO glass plate. After the subsequent UV curing, the sample was immersed in DMF for 10 min to remove the PR and detach the ADCP grating, as shown in Fig. 1A⑤.

In the last stage, $MAPbBr_3$ precursor solution was prepared by dissolving 49.1 mg of MABr and 160.9 mg of $PbBr_2$ into 1 ml of DMF and the solution was stirred for 12 h. The precursor solution with a concentration of 0.21 g/ml was then simply spin-coated onto the ADCP grating at 3,000 rpm for 5 s. The sample was then heated at 90 °C for about 10 s on a hotplate to evaporate the remaining solvent. Confinement of the solution and crystallization in the ADCP microholes produced large-area 2D square lattices of $MAPbBr_3$. The optical microscope image is shown in Fig. S1.

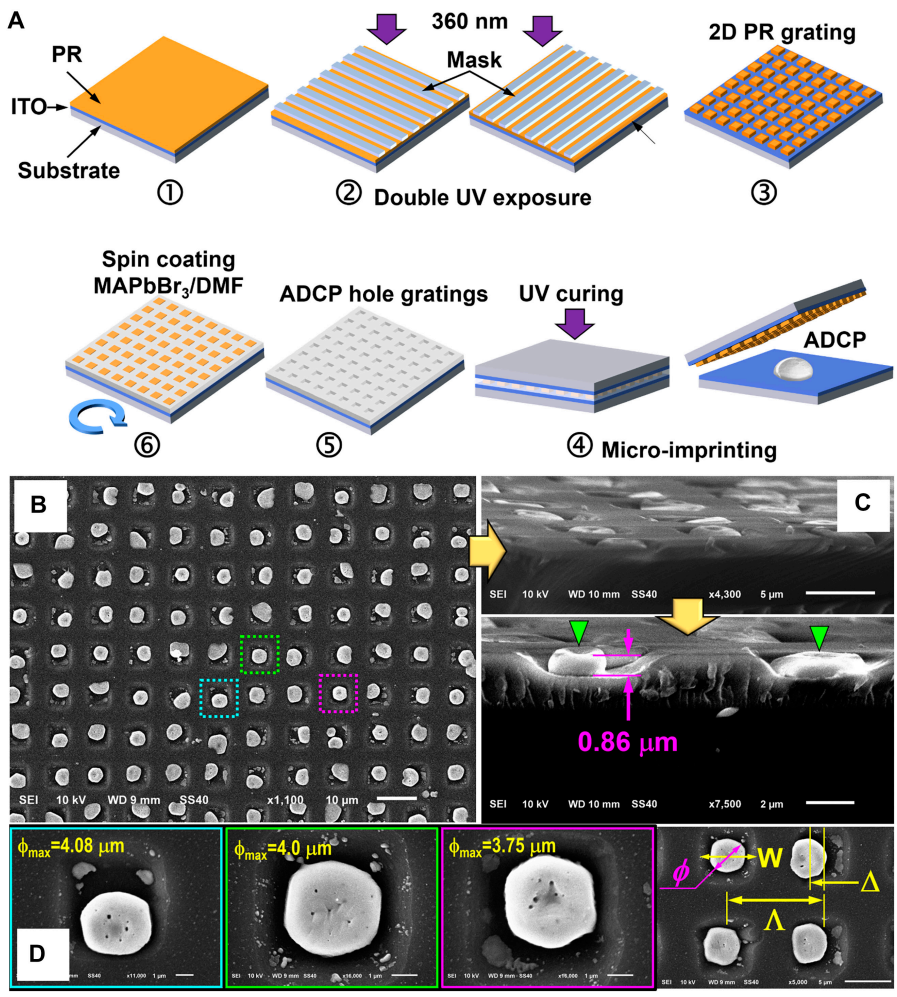

Fig. 1. (A) Fabrication procedures of the 2D lattices of the $MAPbBr_3$ microdisks. (B) SEM image of the 2D lattices of the $MAPbBr_3$ microdisks transferred into the ADCP square-hole gratings. (C) Perspective view of the $MAPbBr_3$ microdisks. (D) Measurement of the maximum diameters of some typical microdisks of polycrystalline $MAPbBr_3$ and definitions of the structural parameters.

Figure 1B shows the scanning electron microscopy (SEM) image of the resultant 2D lattices of multicrystalline $MAPbBr_3$. Randomly sized and randomly shaped multicrystalline disks can be observed, which are confined completely into the lattice holes. The square lattices have a period of 10 μm; however, the randomness in the crystallization process led to the slightly random variation in the lattice constant or the deviation of the disks from the center of the ADCP grating holes. Figure 1C shows a perspective view of the individual $MAPbBr_3$ disks in cross-sectional profiles. Apparently, the disks are in shapes of donuts, although the center hole does not go through the disk body, as indicated by the green triangles in Fig. 1C. The donut-shaped disks have a thickness of about 0.86 μm on the edges.

Figure 1D presents evaluations on single donut disks, locations of which are marked respectively in Fig. 1B. These $MAPbBr_3$ multicrystalline disks are well defined on their boundaries, and their sizes range from 3.75 to 4.08 μm in diameter. Meanwhile, small circular holes are observed, not only implying defects in the multicrystallization scheme but also confirming random scattering structures as random lasing mechanisms both on the crystallization interfaces and around the defect centers. Thus, parameters for characterizing the 2D lattices may include the diameter (ϕ) of the individual disks, lattice period (Λ), side width (W) of the ADCP square hole, and dislocation (Δ) between the centers of the disk and the square hole, as shown in the right panel of Fig. 1D. The relationship of $\phi < W$ and the random value of Δ imply that strong confinement takes place to the precursor solution during the spin-coating process and free crystallization within the ADCP square hole, verifying again the random mechanisms in the formation of the microdisks. As a demonstration of the large-area performance of the 2D lattices, Fig. S1 shows an overview with a dimension of 430 × 320 μm^2 under an optical microscope. As has been investigated in detail in our previous publication [36], the scattering by the interfaces randomly distributed within the freely crystallized microdisks facilitates the dominant mechanism for the random lasing processes in each of the individual microdisk unit. However, the phase locking of these random lasing processes is initialized by what we define as the CASE dynamics.

Principles for Phase Locking of Random Lasers by CASE Dynamics

The CASE dynamics is illustrated schematically by the 2-photon pumped electronic transitions in Fig. 2A. Two-photon excitation (①) by absorbing 2 pumped photons at $h\nu_P$ produces exciton population on the lower edge of the excitation band. Then, the exciton recombination produces emission at $h\nu_e$. Interaction between the emitting photon and the population excitons induces stimulated emissions. The emitted photon will have to experience multiple absorption processes: ② 2-photon absorption by absorbing a pump and an emission photon ($h\nu_P + h\nu_e$), ③ exciton absorption, and ④ ground-state absorption. The internal conversion from the directly excited higher-lying states to the lower edge takes a lifetime of $\Delta\tau$, which is the underlying mechanism for the CASE phase locking. The internal conversion takes shorter than 100 fs in conjugated polymers [37–39]; however, the ground-state relaxation takes more than 300 fs [40]. This lifetime was evaluated to be longer than 300 fs for $MAPbBr_3$ [36]. These 2 time constants determine the constant phase relationship between the CASE cycles.

The 2-photon absorption via ($h\nu_P + h\nu_e$) works only within the overlap between the pump and the probe (emission) pulses; therefore, process ② interacts with the stimulated emission in the early stage, and ③ and ④ become dominant after the pump pulse. However, the electronic transitions via ($h\nu_P + h\nu_e$)

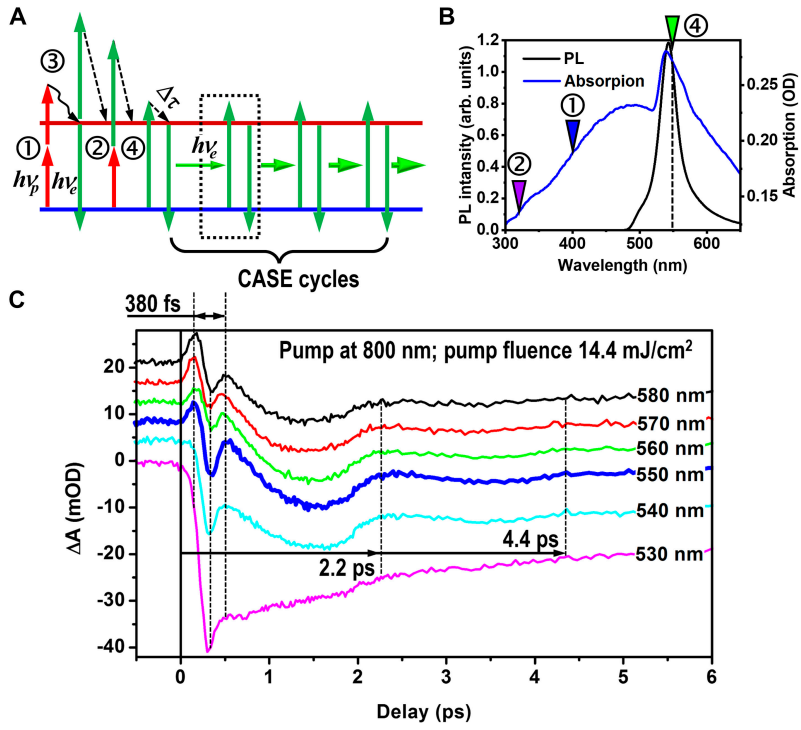

Fig. 2. Principles for the phase locking of random lasing process. (A) Schematic illustration of the CASE cycles. (B) Absorption and emission spectra of patterned $MAPbBr_3$ with correspondence with typical electronic transition processes. (C) Two-photon pumped TA dynamics at wavelengths within the strong absorption and emission bands of $MAPbBr_3$.

corresponds to the absorption highlighted by the triangle in purple in Fig. 2B, which is negligibly small as compared with 2-photon excitation at $2h\nu_p$ (blue triangle) and single-photon absorption at $h\nu_e$ (dashed vertical line). Therefore, we may rule out the possibility of the contribution of $(h\nu_p + h\nu_e)$ to the transient absorption (TA) dynamics.

Moreover, the excitonic absorption takes much longer time than the internal conversion processes. Therefore, process ③ exhibits as a slow modulation on the TA dynamics for the CASE process. As a result, the interaction between ④ and the stimulated emission is dominantly responsible for CASE. Nevertheless, the modulation by process ④ becomes obviously observed after the strong CASE oscillation, as shown in Fig. 2C.

Figure 2C shows the 2-photon (at 800 nm) pumped TA dynamics at typical wavelengths within the strong overlap between the absorption and emission spectra. The pump pulses have a pulse duration of about 150 fs and a pump fluence of 14.4 mJ/cm^2. The TA signal ΔA is calculated by $\Delta A(\lambda,\tau) = -\log_{10}[T_{on}(\lambda,\tau)/T_{off}(\lambda,\tau)]$, where $T_{on}(\lambda,\tau)$ and $T_{off}(\lambda,\tau)$ are the transmission spectra of the probe pulse through the sample with the pump switched on and off, respectively, at a time delay (τ) between the pump and probe pulses. Oscillation dynamics can be clearly observed, in particular, for wavelengths from 540 to 580 nm. At 530 nm, the oscillation feature is not obvious due to the much larger negative signal by stimulated emission and ground-state bleaching than the positive ones by multiple absorption processes. In the early stage, the oscillation exhibits a period of 380 fs. This oscillation is identified as the CASE that is responsible for the phase locking of the random lasing processes.

A slower oscillation is observed with a period of about 2.2 ps after the fast one, as measured in Fig. 2C, where 2 cycles can be observed within the first 6 ps. This oscillation apparently results from the interaction between the exciton absorption and the stimulated emission processes, which becomes weaker with the time delay. Both the 380-fs and the 2.2-ps oscillation are most prominently observed at 550 nm, where the best phase-locked lasing performance is observed, as will be demonstrated in the following sections. However, the fast oscillation at the early stage of the TA dynamics is much stronger than the slow one, which plays a dominant role in determining the time constant for the CASE dynamics [36]. Therefore, the TA dynamics in Fig. 2C supplies verification of our proposed CASE mechanism in Fig. 2A. Thus, although 2-photon excitation produced more complex absorption processes, the single-photon absorption by the ground state is still the most important process responsible for the phase locking and the time constant is determined by internal conversions.

Such an oscillatory modulation can also be observed in the single-photon-pumped TA dynamics, as shown in Fig. S2. The 150-fs pulses at 400 nm were used as the pump and the supercontinuum pulses as the probe, where the pump is located within the absorption spectrum for direct single-photon excitation. Multiple stages can be observed within the negative TA dynamics curve, as guided by the dashed lines. These oscillation features result from the competition among multifold absorption, stimulation emission, and the ground-state absorption bleaching (GSAB) processes. Different from 2-photon excitation, single-photon process involves more contribution from the GSAB process due to the strong single-photon absorption. Clearly, the oscillation also has a rough period of about 380 fs, agreeing well with the case for 2-photon excitation. This period is longer than that reported in our previous publication in [36], implying slight modification of the energy-band structures due to the much different multicrystalline structures and the consequent small change in the internal conversion lifetime. Nevertheless, the single-photon TA dynamics not only verifies further the phase-locking mechanism but also determines the time constant for internal conversions, which equals roughly that resolved by the 2-photon scheme.

Phase-Locked Random Lasing by CASE Dynamics

The random lasing performance is investigated using a micro-spectroscopic system, as depicted in Fig. 3A. The 150-fs laser pulses at 800 nm with a repetition rate of 1 kHz are sent to the sample of $MAPbBr_3$ microdisks through reflection by a dichroic mirror and focusing by a 50× objective. The excitation laser spot has a diameter of roughly 10 μm. The emission in the green is recollimated and sent to the spectrometer after passing through the dichroic mirror and being collected by a fiber that is connected to a SpectraPro HRS-500 spectrometer. The core diameter of the collection fiber is 600 μm, outside which is a ring illumination by a halogen lamp to indicate the collection area on the sample. The position of the collection end of the fiber can be adjusted to choose the interested positions on the sample. The size of the collection area was determined by the magnification of the objective lens and the core diameter of the fiber, which is about 12 μm for the experimental results. Since both the excitation laser spot and the collection area can only cover a single $MAPbBr_3$ disk, we do not need to consider intercoupling between different lattice sites and our investigations are focused on the random lasing properties inside each individual lattice site.

Figure 3B shows an optical microscopic image of the 2D lattices of $MAPbBr_3$ disks, where 2 lattice sites A and B are chosen for the random lasing investigation, as highlighted by red circles. These 2 disks have a complete circular disk shape and a typical size among the lattice sites, which is about 4.4 μm in diameter. Although the periodic arrangement of the lattice sites is somewhat destroyed during the fabrication process, the mean separation distance between them is still about 10 μm so that sites A and B can be pumped individually by the laser spot.

Compared with single-photon pumping, the 2-photon scheme allows larger penetration depth of the pump photons into the disk body, inducing more random lasing channels. According to our modeling on phase-locking processes in [36], the phase-locked lasing intensity at a center wavelength λ can be calculated by:

$$I(\lambda) = \left| \sum_{m=1}^{N} E_m(\lambda) e^{jm\Delta\phi\lambda} \right|^2 \quad (1)$$

where N is the number of cascading cycles and is also correlated directly to the number of random lasing modes that are locked in phase, $E_m(\lambda)$ is the optical electric field of mode m, and $\Delta\phi$ is the constant phase shift between 2 adjacent CASE cycles, which is determined by the internal relaxation time constant as:

$$\Delta\phi = \frac{2\pi}{\lambda}\Delta\tau \bullet c \quad (2)$$

with $\Delta\tau$ defined as the relaxation lifetime of the excited molecules to the lower edge of the excitation band and c as the velocity of light in vacuum. The large increase in the value of N will lead to much narrowed lasing linewidth [36].

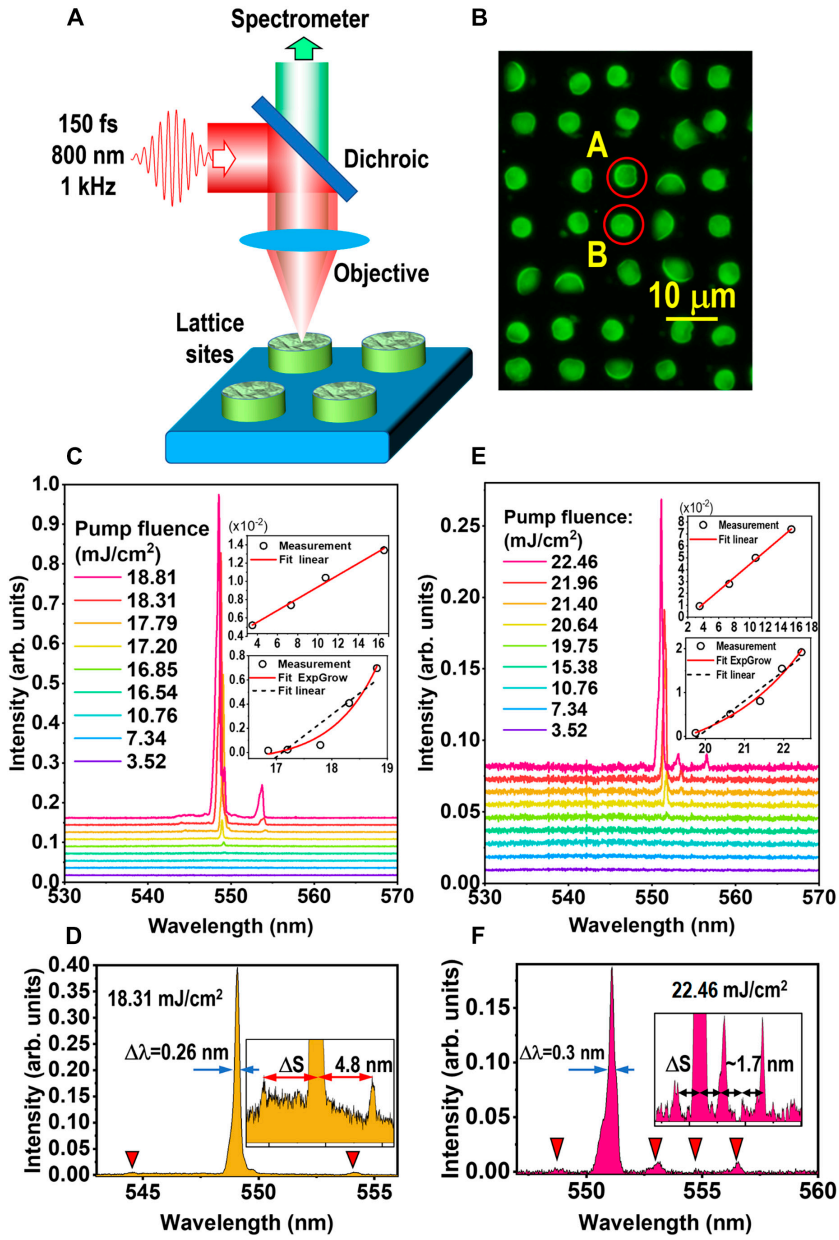

Fig. 3. Phase-locked random lasing by 2-photon pumping. (A) Experimental setup for femtosecond 2-photon microspectroscopy. (B) 2D lattices of microdisks of polycrystalline $MAPbBr_3$. (C and D) Phase-locked random lasing performance for lattice site A in (B). (E and F) Phase-locked random lasing performance for lattice site B in (B).

Figure 3C and D shows the phase-locked random lasing properties on lattice site A. Narrow lasing lines with equal separation can be observed for all spectra measured above the pump threshold, evidencing the phase-locking relationship between the lasing modes. Figure 3C shows the lasing spectra as the pump fluence is increased from 3.52 to 19.75 mJ/cm^2, with the lasing intensity at the main peak of 548.8 nm plotted as a function of the pump fluence in the insets. The background photoluminescence (PL) spectrum has been subtracted from all of the lasing spectra so that pure lasing lines with high contrasts can be observed. The lasing spectra before the removal of the PL background are shown in Fig. S3. Three lasing lines can be observed at a center wavelength of about 544, 548.8, and 553.6 nm, where the mode at 548.8 nm is much stronger than the other 2, due to its spectral location with a best balance between the absorption and emission. Relatively weaker absorption and stronger emission favors stronger lasing intensities. Therefore, the strongest lasing line tends to appear at the most favorable balancing between the overlapped emission and absorption spectra. Slight blue-shift can be observed for all the 3 lasing lines by increasing the pump fluence. Due to the strong overlap between the absorption and emission spectra, as shown in Fig. 2B, by increasing the pump fluence, the ground-state absorption by the gain medium is reduced so that lasing action becomes allowed for spectral positions with previously stronger absorption. Meanwhile, the emission becomes stronger and tends to shifts toward the peak intensity of the PL spectrum. However, the lasing lines are all at longer wavelengths than the peak absorption and the peak emission, as shown in Fig. 2. Thus, the lasing lines tend to shift to the blue by increasing the pump fluence. This not only verifies the

balancing effect but also evidences further the phase-locking relationships between these lasing modes. Furthermore, the balancing effect is responsible for the slight inequality in the separation between the lasing lines.

The insets of Fig. 3C show plots of the emission intensity at 548.8 nm as a function of pump fluence, where we have a linear dependence before reaching the lasing threshold for the pump fluence lower than 16.54 mJ/cm^2 and an exponential growth dependence after exceeding the threshold for the pump fluence higher than 16.85 mJ/cm^2. The nonlinearity is clearly verified by the comparison with the linear fitting (dashed black line) to the measurement data. Such a nonlinear dependence has also been observed for single-photon pumping scheme, which is considered to be the characteristic of the phase-locked random lasers [36]. It is understandable that the observed lasing spectrum at the output results from the coherent overlap between different lasing modes, which are correlated with fixed phase relationship. This mechanism is different from the conventional mode locking, since the randomness in the lasing modes makes them competitive, instead of constructive coupling with each other.

Furthermore, such phase-locking effect in random lasers can only be observed in a very limited area defined by the overlap between the small pumping laser spot and the small $MAPbBr_3$ disk, which is a few micrometers in diameter. For large-area pumping, the phase-locking effect cannot be observed due to the larger number of the random lasing channels so that a broadband lasing spectrum is generally observed. In this case, the broad lasing spectrum should not be simply identified as amplified spontaneous emission (ASE); instead, it is a result of an overlap of a large number of random lasing lines. An experimental result as a verification is shown in Fig. S4, where the pump laser pulses at 800 nm have a beam diameter larger than 3 mm.

Figure 3D replots the laser spectrum at a pump fluence of 18.31 mJ/cm^2, where the linewidth and the mode separation can be precisely measured. The central line at 548.8 nm has a bandwidth of $\Delta\lambda = 0.26$ nm at full width at half maximum (FWHM), and it is located at the symmetric center between the other 2 with an equal separation of $\Delta S \approx 4.8$ nm. Such a spectral separation corresponds to a cavity length of larger than 63 μm, if assuming lasing actions in whispering galley microcavities. However, the diameter of lattice site A is only 4.4 μm, corresponding to a circumference smaller than 14 μm, which in no way produces a whispering gallery mode as defined by the above parameters. Additionally, the irregular shape and the defects in the microdisks cannot support the microcavity oscillating modes.

According to the optical microscopic image in Fig. 3B, much brighter center is observed for lattice site B than for A, implying that B has a larger thickness than A. Therefore, more random lasing channels are possibly involved in the phase-locking processes. It is understandable that larger volume of the active material leads to the increase in N and possibly simultaneous phase locking of multiple channels. These features are well demonstrated in the lasing performance in Fig. 3E and F. In Fig. 3E, we show the phase-locked random lasing spectra as the pump fluence is increased from 3.52 to 26.5 mJ/cm^2, where the PL background has been subtracted. The lasing spectra before the removal of the PL background are shown in Fig. S5. Multiple lasing lines are observed simultaneously with the strongest centered at about 551 nm. Similarly, the slight blue-shift effect can also be observed for all of the lasing lines. According to the insets of Fig. 3E, the lasing threshold is about 19.75 mJ/cm^2, which is much higher than that for lattice site A, confirming the larger thickness and the more complicated structures in the disk on site B. An exponential growth dependence is again observed for the lasing intensity as a function of the pump fluence that is higher threshold, as shown in the insets of Fig. 3E.

Figure 3F shows the lasing spectrum evaluating the linewidth and mode separation for the phase-locked lasing modes, where we measure a bandwidth of about 0.3 nm at FWHM for the central lasing line at about 551 nm and an equal separation of about 1.7 nm for the 5 modes. Such a smaller mode separation rules out further the possibilities of whispering gallery modes, since the corresponding microcavity length needs to be larger than 177 μm; however, the diameter of the lattice site B is also about 4.4 μm.

For further verification of the dependence on the dimensions of the microdisks, we carried out measurements on some more lattice sites, as shown in Figs. S6 and S7. Although there is indeed some variation in the linewidth and mode separation, as compared with Fig. 3, the linewidth is basically within the small range of 0.26 to 0.4 nm, which implies a constant internal transition lifetime. Furthermore, increasing the thickness of the microdisks with the same diameter will also increase the number of random lasing channels to be phase-locked, leading to possibly more lasing modes. Moreover, a lasing mode is missing in Fig. S7, as indicated by a dashed vertical line. This supplies further evidence for the phase-locked interference between simultaneous random lasing modes. The fixed phase relationship plays an important role in determining the final intensity of each lasing line at a different wavelength.

Conclusion

We report phase-locked random lasing in patterned $MAPbBr_3$, where we fabricated large-area arrays of microdisks in donut shapes and employed 2-photon pumping at 800 nm with a pulse duration of 150 fs. Multiple laser modes work simultaneously with locked phase relationships to produce a lasing line width as narrow as 0.26 nm at FWHM with equal spectral separations. The central physics for this mode-locking scheme is the CASE, which is the most significant contribution of this investigation to laser physics and random lasers. Compared with single-photon pumping, the 2-photon scheme enables large penetration depth of the pump pulses into the active medium with patterned structures and consequently largely extended random lasing channel length or largely increased phase-locking volume. This leads to significantly reduced linewidth and enhanced contrast of the lasing lines. The discovered physics and related investigations push forward the advancement of both the random lasers and laser mode-locking technologies.

Acknowledgments

Funding: This work was supported by the National Natural Science Foundation of China (12074020).
Author contributions: Q.Z. carried out the fabrication of the structures, optical spectroscopic measurements, and microscopic measurements. Y.L., Y.Z, and Y.X.Z. helped with the optical spectroscopic measurements and the design of the optical measurement system. J.X.G and Y.W.Z. supplied support to spectroscopic and microscopic measurements, femtosecond laser system

maintenance. Y.L.F. managed the micro-spectroscopic system and supervised the micro-spectroscopic measurements. X.P.Z. designed this research, did the data processing and analysis, supplied resources supporting this work, supervised this research, and wrote this paper.

Competing interests: The authors declare that they have no competing interests.

Data Availability

Data are available on request from the corresponding authors.

Supplementary Materials

Figs. S1 to S7

References

1. Fruhling C, Wang K, Chowdhury S, Xu XH, Simon J, Kildishev A, Dou LT, Meng XG, Boltasseva A, Shalaev VM. Coherent random lasing in subwavelength quasi-2D perovskites. *Laser Photonics Rev*. 2023;17(4):2200314.
2. Weng GE, Tian J, Chen SM, Xue JJ, Yan JY, Hu XB, Chen SQ, Zhu ZQ, Chu JH. Giant reduction of the random lasing threshold in $CH_3NH_3PbBr_3$ perovskite thin films by using a patterned sapphire substrate. *Nanoscale*. 2019;11(22):10636–10645.
3. Roy PK, Ulaganathan RK, Raghavan CM, Mhatre SM, Lin HI, Chen WL, Chang YM, Rozhin A, Hsu YT, Chen YF, et al. Unprecedented random lasing in 2D organolead halide single-crystalline perovskite microrods. *Nanoscale*. 2020;12(35):18269–18277.
4. Chirvony VS, Suárez I, Sanchez-Diaz J, Sánchez RS, Rodríguez-Romero J, Mora-Seró I, Martínez-Pastor JP. Unusual spectrally reproducible and high Q-factor random lasing in polycrystalline tin perovskite films. *Adv Mater*. 2023;35(9):2208293.
5. Liang HK, Yu SF, Li XF, Ma SZ, Yang HY. An index-guided ZnO random laser array. *IEEE Photon Technol Lett*. 2011;23(8):522–524.
6. Yang ZJ, Zhang WL, Ma R, Dong X, Hansen SL, Li XF, Rao YJ. Nanoparticle mediated microcavity random laser. *Photonics Res*. 2017;5(6):557–560.
7. He QS, Chen DD, Wan Q, Pi MY, Wu JW, Zhang P, Zhang DK. Plasmonically enhanced random lasing emission based on Ag scattered nanofiber networks. *Opt Laser Technol*. 2019;116:26–30.
8. Rashidi M, Haggren T, Su ZC, Jagadish C, Mokkapati S, Tan HH. Managing resonant and nonresonant lasing modes in GaAs nanowire random lasers. *Nano Lett*. 2021;21(9):3901–3907.
9. Redding B, Choma MA, Cao H. Speckle-free laser imaging using random laser illumination. *Nat Photonics*. 2012;6(6):355–359.
10. Wang YC, Li H, Hong YH, Hong KB, Chen FC, Hsu CH, Lee RK, Conti C, Kao TS, Lu TC. Flexible organometal-halide perovskite lasers for speckle reduction in imaging projection. *ACS Nano*. 2019;13(5):5421–5429.
11. Mallick SP, Sung Z. Holographic image denoising using random laser illumination. *Ann Phys-Berlin*. 2020;532(12):2000323.
12. Liu YL, Yang WH, Xiao SM, Zhang N, Fan YB, Qu GY, Song QH. Surface-emitting perovskite random lasers for speckle-free imaging. *ACS Nano*. 2019;13(9):10653–10661.
13. Hou Y, Zhou ZH, Zhang CH, Tang J, Fan YQ, Xu FF, Zhao YS. Full-color flexible laser displays based on random laser arrays. *Sci China Mater*. 2021;64(11):2805–2812.
14. Wang Q, Tong Y, Ye HT, Liang XJ, Yang KQ, Xiang WD. Dual-protective $CsPbX_3$ perovskite nanocomposites with improved stability for upconverted lasing and backlight displays. *ACS Sustain Chem Eng*. 2021;9(34):11548–11555.
15. Jin MFF, Gao W, Liang XJ, Fang Y, Yu SF, Wang T, Xiang WD. The achievement of red upconversion lasing for highly stable perovskite nanocrystal glasses with the assistance of anion modulation. *Nano Res*. 2021;14(8):2861–2866.
16. Li RX, Yu JH, Wang S, Shi YQ, Wang ZJ, Wang K, Ni ZH, Yang XY, Wei ZP, Chen R. Surface modification of all-inorganic halide perovskite nanorods by a microscale hydrophobic zeolite for stable and sensitive laser humidity sensing. *Nanoscale*. 2020;12(25):13360–13367.
17. Lin ST, Wan ZA, Qi YF, Han B, Wu H, Rao YJ. Wideband remote-sensing based on random fiber laser. *J Lightwave Technol*. 2022;40(9):3104–3110.
18. Wang CC, Kataria M, Lin HI, Nain A, Lin HY, Inbaraj CRP, Liao YM, Thakran A, Chang HT, Tseng FG, et al. Generation of silver metal nanocluster random lasing. *ACS Photonics*. 2021;8(10):3051–3060.
19. Sato R, Henzie J, Zhang BY, Ishii S, Murai S, Takazawa K, Takeda Y. Random lasing via plasmon-induced cavitation of microbubbles. *Nano Lett*. 2021;21(14):6064–6070.
20. Zhu HY, Zhang WL, Zhang JC, Ma R, Wang Z, Rao YJ, Li XF. Single-shot interaction and synchronization of random microcavity lasers. *Adv Mater Technol*. 2021;6(9):2100562.
21. Monroy L, Soriano-Amat M, Esteban Ó, Monroy E, González-Herráez M, Naranjo FB. Performance enhancement of an ultrafast all-fiber laser based on an InN saturable absorber using GRIN coupling. *Opt Express*. 2021;29(18):29357–29365.
22. Yang S, Li JZ, Li L, Zhang L, Zhang XW. Mode-locking operation of an Er-doped fiber laser with $(PEA)_2(CsPbBr_3)_{n-1}PbBr_4$ perovskite saturable absorbers. *J Mater Chem C*. 2022;10(19):7504–7510.
23. Pang LH, Zhao M, Zhao QY, Li L, Wang RF, Wu RQ, Lv Y, Liu WJ. GaSb film is a saturable absorber for dissipative soliton generation in a fiber laser. *ACS Appl Mater Interfaces*. 2022;14(50):55971–55978.
24. Liu SX, Li G, Zhu F, Huang HF, Lu JS, Qu JL, Li L, Wen Q. $GeAs_2$ saturable absorber for ultrafast and ultranarrow photonic applications. *Adv Funct Mater*. 2022;32(17):2112252.
25. Rafique MZE, Basiri A, Bai J, Zuo JW, Yao Y. Ultrafast graphene-plasmonic hybrid metasurface saturable absorber with low saturation fluence. *ACS Nano*. 2023;17(11):10431–10441.
26. Liu JT, Ye S, Guo HW, Yao YP, Zhou X, Nie HK, Wang RH, Yang KJ, He JL, Zhang BT. Enhanced ultrafast dynamics and saturable absorption response of Nb_2SiTe_4/graphene heterostructure for femtosecond mode-locked bulk lasers. *Opt Laser Technol*. 2023;166:Article 109635.
27. Yang YM, Li HY, Zhang HN, Chen XH, Li P. Triple-wavelength mode-locked laser based on a $Cr_2Si_2Te_6$ saturable absorber. *Opt Fiber Technol*. 2023;76:Article 103223.
28. Liu WJ, Xiong XL, Liu ML, Xing XW, Chen HL, Ye H, Han JF, Wei ZY. Bi_4Br_4-based saturable absorber with robustness at high power for ultrafast photonic device. *Appl Phys Lett*. 2022;120(5):Article 053108.
29. Zhang X, Xing XW, Li J, Peng XL, Qiao L, Liu YX, Xiong XL, Han JF, Liu WJ, Xiao WD, et al. Controllable epitaxy of

quasi-one-dimensional topological insulator α-Bi_4Br_4 for the application of saturable absorber. *Appl Phys Lett*. 2022;120(9):Article 093103.
30. Guo Q, Pan J, Liu Y, Si H, Lu Z, Han X, Gao J, Zuo Z, Zhang H, Jiang S. Output energy enhancement in a mode-locked Er-doped fiber laser using CVD-Bi_2Se_3 as a saturable absorber. *Opt Express*. 2019;27:24670–24681.
31. Xing X, Liu Y, Han J, Liu W, Wei Z. Preparation of high damage threshold device based on Bi_2Se_3 film and its application in fiber lasers. *ACS Photonics*. 2023;10:2264–2271.
32. Leonetti M, Conti C, López C. Dynamics of phase-locking random lasers. *Phys Rev A*. 2013;88(4):Article 043834.
33. Antenucci F, Lerario G, Fernandéz BS, De Marco, De Giorgi, Ballarini D, Sanvitto D, Leuzzi L. Demonstration of self-starting nonlinear mode locking in random lasers. *Phys Rev Lett*. 2021;126(17):Article 173901.
34. Leonetti M, Conti C, López C. The mode-locking transition of random lasers. *Nat Photonics*. 2011;5(10):615–617.
35. Di Gaspare A, Pistore V, Riccardi E, Pogna EAA, Beere HE, Ritchie DA, Li LH, Davies AG, Linfield EH, Ferrari AC, et al. Self-induced mode-locking in electrically pumped far-infrared random lasers. *Adv Sci*. 2023;10(9):2206824.
36. Zhang XP, Hu JY, Fu YL, Guo JX, Zhang YW, Song XY. Phase-locking of random lasers by cascaded ultrafast molecular excitation dynamics. *Laser Photonics Rev*. 2023;17(3):2200333.
37. Jespersen KG, Yartsev A, Pascher T, Sundström V. Excited state dynamics in alternating polyfluorene copolymers. *Synth Met*. 2005;155(2):262–265.
38. Harrison MG, Urbasch G, Mahrt RF, Giessen H, Bässler H, Scherf U. Two-photon fluorescence and femtosecond two-photon absorption studies of MeLPPP, a ladder-type poly(phenylene) with low intra-chain disorder. *Chem Phys Lett*. 1999;313(5-6):755–762.
39. Gadermaier C, Lanzani G. Photophysics of conjugated polymers: The contribution of ultrafast spectroscopy. *J Phys Condens Matter*. 2002;14:9785–9802.
40. Lanzani G, Cerullo G, Polli D, Gambetta A, Zavelani-Rossi M, Gadermaier C. Photophysics of conjugated polymers: The contribution of ultrafast spectroscopy. *Phys Stat Sol A*. 2004;201(6):1116–1131.